Feasibility analysis of the performance of low-cost GNSS receivers in monitoring dynamic motion

Chenyu Xue [a,*], Panos A. Psimoulis [a], Xiaolin Meng [b]

[a] *Nottingham Geospatial Institute, University of Nottingham, UK*
[b] *Beijing University of Technology, China*

A R T I C L E   I N F O

A B S T R A C T

The development of low-cost GNSS receivers broadens their applications, such as deformation monitoring, which have been performed routinely by survey-grade GNSS receivers. To evaluate the performance of low-cost GNSS receivers, we assessed the precision of low-cost multi-GNSS receivers in monitoring dynamic motion and developed methods of using a closely-spaced dual low-cost GNSS receivers' system to enhance their performance. In this study, both the survey-grade and low-cost GNSS receiver/antennas were mounted on a circular rotating device executing controlled periodic rotation. It was shown that the precision of the low-cost GNSS receivers could be enhanced to the level of 2–4 mm, by using multi-GNSS observations and limiting the noise level based on error modelling and filtering of the closely–spaced low-cost GNSS receivers. Finally, from the experiments and a real bridge monitoring application, it was proved that low-cost GNSS receivers could accurately define modal frequencies of ~0.362 Hz and ~1.680 Hz, respectively.

1. Introduction

Structural health monitoring (SHM) is of significant importance to ensure the safe function and efficient maintenance of civil engineering infrastructures. GNSS technology is a method which provides accurate, continuous, and reliable measurements in independent global coordinate system, reflecting the overall response of the structure and not the locally relative behaviour of structure components [1]. For the last two decades, geodetic GNSS receivers/antennas have been deployed for geodetic monitoring purposes achieving millimetre accuracy [2,3,4,5], with bridge SHM being one of the major areas [6,7]. GNSS technology has been applied in permanent monitoring systems of bridges, such as the Tsing Ma Bridge [8] and Forth Road Bridge [6]. The continuous development and advancements of satellite systems (i.e., Galileo, Bei-Dou, etc.) have led to the enhanced accuracy of GNSS measurements and the development of methodologies for efficient estimation of bridge response [7,9]. However, the high deployment cost restricted its broader application, especially when multiple locations in a monitoring network are of interest and when the monitoring equipment is subjected to adverse monitoring conditions.

Until recent years, the advancement in GNSS receiver technology has made some mass–market low-cost (consumer-grade) GNSS receivers competitive in precise carrier phase observations with high-frequency sampling rate (up to 10 Hz) and multi-GNSS tracking. These features have made precise positioning (either by RTK or PPP) possible with low-cost GNSS receivers, especially due to their capability for precise carrier phase observations. Compared to survey-grade GNSS receivers, the low-cost GNSS receivers are light-weight, compact, smaller, and priced ten to twenty times lower than a typical geodetic GNSS receiver. Although there is a trend with more low-cost GNSS receivers being manufactured to measure in dual frequency band (e.g., u-blox ZED-F9P), the low-cost GNSS receiver market is still dominated by single-frequency consumer-grade GNSS devices in the current stage [10], and their performances are compromised in functions, such as preamplifier, front end, digital signal processing (DSP) and low noise amplifier (LNA), which lead to a higher receiver measurement noise and less multipath suppression capability [11]. Compared with dual/multi-frequency measurements, single-frequency observation indicates firstly the inapplicability of iono-spheric free linear combination, secondly poor ambiguity resolution performance such as extended ambiguity resolution time [10], and thirdly the increased probability of cycle-slip occurrence. Therefore, its drawback should be noted, especially for longer baselines, in mobile environments where cycle slips occur frequently, and in real-time.

Previous studies have been conducted to evaluate the performance of

* Corresponding author.
  E-mail address: evxcx1@outlook.com (C. Xue).

low-cost GNSS receivers. Takasu and Yasuda [12] evaluated the RTK GPS performance with several types of low-cost single-frequency GNSS receivers against survey-grade geodetic receivers in terms of positioning accuracy, fix-rate, and time to first fix (TTFF) for ambiguity resolution. Even though major differences were detected between using geodetic-grade and consumer-grade antennas, RTK results of similar accuracy were obtained between geodetic-grade and consumer-grade receivers due to their similar carrier phase multipath level. Based on RTK GPS tests, Takasu and Yasuda [13] concluded that the low-cost GNSS receivers could reach a comparable performance with single-frequency geodetic grade receiver. Cina and Piras [14] also concluded that for GPS post-processing, under favourable circumstances, such as long acquisition time, short baseline length and use of an external antenna, the differences between consumer-grade (u-blox 5 T) and geodetic grade receivers are not large. It is also reported by Garrido-Carretero et al. [15] that low-cost receivers can reach a comparable positioning performance to survey-grade receivers in real-time positioning for short baselines. Furthermore, the study of Jo et al. [16] showed that C/A (Coarse Acquisition) code low-cost receivers could be used for high precision in dynamic response of 20–30 cm, with further accuracy improvement if more sensors were adopted.

Based on the experimental studies of low-cost GNSS receivers, it is generally shown that centimetre or sub-centimetre level precision could be achieved with relative positioning for baseline up to 10 km by using single-frequency observations of low-cost receivers [13,14,15,17,18,19,20], and a higher precision could be achieved with an external geodetic or choke-ring antenna other than with the patch antenna [14,21]. The incorporation of multi-GNSS observations with single frequency low-cost GNSS receiver was also extensively investigated by either using GPS + BeiDou [22,23] or GPS + QZSS + BeiDou + Galileo [24,25,26], achieving mm to cm-level positioning in short baseline comparable to the more expensive dual frequency receivers. In the RTK analysis of low-cost GNSS receivers, the impact of residual atmospheric delays on different baseline length was investigated by Odolinski and Teunissen [24,25,26], where the relative slant ionospheric delays and tropospheric delays could be ignored providing short baseline (i.e., few km) and should be modelled as unknown parameters as a function of baseline length for long baselines. Furthermore, some zero–baseline experimental studies investigated the noise level of low-cost GNSS receivers and the impact of GNSS antenna [27,28], whereas other short-baseline experimental studies investigated methods to decrease the noise level of low-cost GNSS receivers based on spatially correlated GNSS measurements [28,29].

However, most low-cost GNSS experimental studies focused on the performance of stable low-cost GNSS receivers, simulating their performance for applications in static or quasi-static deformation monitoring conditions, such as tectonic motion and landslide [14,17,30,31,32]. A few studies have focused on the investigation of the performance of low-cost GPS/GNSS receivers monitoring dynamic motion. More specifically, Jo et al. [16] assessed the accuracy of chipset low-cost GPS receiver in slow dynamic motion based on circular motion experiments; Benedetti et al. [33] assessed low-cost u-blox GPS receiver as part of a low-cost monitoring system in monitoring one-degree dynamic motion of a shaking table; Lăpădat et al. [34] assessed the accuracy of low-cost dual-frequency GNSS receiver (u-blox ZED-F9P) monitoring dynamic motion using though only GPS measurements; Manzini et al. [35] evaluated the performance of low-cost GNSS receiver with 1-Hz sampling rate, in dynamic motion experiments of oscillation frequency up to 0.25 Hz.

Furthermore, in very limited studies, low-cost GNSS receivers have been applied in bridge monitoring. Poluzzi et al. [19] assembled a low-cost GNSS sensor monitoring system on a 94–m bridge focusing mainly on the mitigation of the low-frequency noise of the GNSS measurements due to multipath, without though assessing the performance in monitoring the dynamic response of the bridge. Manzini et al. [35] also tested a network of 1 Hz low-cost GNSS stations deployed on a suspension bridge to validate their performance by correlating with other displacement traditional sensors.

The aim of this study was to assess the performance of low-cost consumer grade GNSS receivers based on dynamic displacement detection by controlled experiments and a case study of bridge monitoring. Firstly, we examined the impact of different parameters, such as (i) the amplitude of the dynamic motion, (ii) the antenna/receiver type of the base station, and (iii) the adopted satellite system (GPS only or GPS + Galileo multi-GNSS), on the precision of the low-cost GNSS solution. Also, we evaluated the potential enhancement of the low-cost GNSS receiver performance, by deploying two closely-spaced identical low-cost GNSS receivers and adopting three different strategies in order to combine the GNSS time-series of the two receivers and mitigate the GNSS errors' impact on the final low-cost GNSS displacement time-series. In all cases, the performance of the low-cost GNSS receiver(s) was assessed against geodetic-grade GNSS receiver. Then, the low-cost GNSS receivers were examined in deformation monitoring of the Wilford Suspension Bridge, evaluating the accuracy in estimating the dynamic response (amplitude and frequency) of the bridge against the geodetic-grade GNSS receiver and Robotic Total Station (RTS). Hence, a holistic approach is adopted in the current study, based on experimental assessment of the low-cost GNSS receivers followed by the case study, which was not followed in any of the previous studies focusing on the monitoring of dynamic motion using low-cost GNSS receivers.

2. Methodology

To assess the performance of low-cost GNSS receivers, experiments with controlled circular motion were conducted. The dynamic circular controlled motion GNSS experiments is an approach extensively applied in several previous studies for the assessment of GNSS performance in monitoring displacement of flexible civil engineering structures [16,36,37,38]. The main advantage of this experimental set-up is that the low-cost and geodetic-grade GNSS receivers execute the same motion with the same measuring/environmental conditions on predefined circular trajectories of known radius. Different radius of circular motions similar to those of previous studies (ranging between 5 and 50 cm [16,36,37]) were examined to evaluate the impact of the amplitude of the dynamic motion on the precision of low-cost GNSS receivers. The range of the examined radiuses are generally in agreement with the response of flexible bridges [6,9]. Also, the rotation period of around 3 s matches the rotation period of previous similar studies [16,36] and it is in the range of modal frequencies of flexible civil engineering structures, such as long-span bridges.

The GNSS measurements were post-processed in kinematic mode using the Double Difference technique (DD) in order to cancel biases such as satellite orbit error, receiver clock error and mitigate the ionospheric and tropospheric errors effectively [39]. The remaining errors are uncorrelated between the rover and base station, such as site-dependent errors (multipath error), antenna dependent errors (PCV and PCO) and systematic noise due to cable, receiver, and antenna [28]. The multipath error is expected to be largely suppressed due to the dynamically moving antenna.

Several parameters were examined to investigate approaches which can be applied to enhance the performance of low-cost GNSS receivers in monitoring dynamic motion. Firstly, the performance of low-cost GNSS receivers was investigated for:

(i) Four different grades of GNSS base stations to assess the impact of the GNSS base station on the solution of the low-cost GNSS receiver. The GNSS base station consisted of (a) a geodetic-grade antenna with a dual-frequency geodetic GNSS receiver; (b) a geodetic-grade antenna with a low-cost GNSS receiver; (c) a patch antenna with a low–cost GNSS receiver; and d) a patch antenna with a geodetic receiver.

(ii) Two different GNSS constellation solutions to evaluate the potential beneficial impact of additional satellite systems (i.e., Galileo) on the performance of low-cost GNSS receivers. The examined GNSS solutions are (a) GPS-only solution and (b) GPS + Galileo multi-GNSS solution.

(iii) Different radius of circular motion, to assess the impact of the motion amplitude on the precision of the GNSS displacement time-series.

Then, the approach of combining two closely-spaced (i.e., 20 cm) low-cost receivers was investigated, aiming to limit the impact of potential common errors of the two receivers and enhance the GNSS time-series precision. This approach was examined and successfully applied in static measurements in the study of Xue et al. [28]. Three strategies were applied to analyse the two GNSS receivers time-series and estimate the GNSS displacement time-series:

(a) Averaging the GNSS solutions of the two closely-spaced low-cost GNSS receivers, aiming to limit the GNSS data errors, since both low-cost GNSS receivers execute the same motion. This approach was tested successfully with a dense array of low-cost GNSS receivers, where averaging their measurements reduced the GNSS noise level [16].

(b) Application of high-pass filter independently to the GNSS time-series of the two low-cost receivers aiming to limit the impact of low-frequency noise of the GNSS data, such as multipath; an approach broadly applied in GNSS time-series analysis [7,28,40]. After filtering, the two GNSS displacement time-series were averaged to improve the precision of the final GNSS displacement time-series potentially further.

(c) Application of the common-mode-error (CME) filtering technique on the two closely–spaced low-cost GNSS receivers [28]. This strategy was based on the assumption that closely-spaced GNSS receivers are spatially correlated and potentially include common errors characterising mainly the low-frequency band (i.e., <0.1 Hz), such as multipath [28,41]. Hence, the aim was to model potential common low-frequency noise of the GNSS time-series of the two low-cost receivers, and then subtract it from the GNSS time-series [42,43]. Then again the two GNSS time-series were averaged to improve even further the precision of the final low-cost GNSS time-series.

It should be mentioned that the spacing between the two patch antennas should not be too close since this will lead to near-field mutual coupling, which could cause poor impedance and radiation performance [44]. The main rule is that the spacing between two antennas spacing for constructing array antennas is usually half-wavelength of the signal [44]. In the experimental lay-out the distance between the two low-cost antennas was ~20 cm, exceeding the requirement of half-wavelength for the GPS L1 signal (i.e., 19 cm wavelength for L1 carrier), and sufficiently reducing the mutual coupling impact. Similar approach of closely-spaced low–cost GNSS receivers has also been adopted in previous studies [29,41].

3. Experiments

The experiments were carried out in January and March of 2020 on the roof of Nottingham Geospatial Institute (NGI) to limit potential obstacles and increase the number of available satellites (Fig. 1). We followed the same design for the deployment of the GNSS receivers as for the short baseline experiments described in Xue et al. [28], where the base station was located at pillar NGB5 and the rover stations at ~20 m distance, at pillar NGB3.

For the base station, a geodetic antenna (Leica AS10) and an active low noise/high gain coverage ANN-MS patch antenna with SMA connector (from the u-blox EVK-M8T Evaluation Kit) were adopted for respective measurements in January and March 2020 to examine the impact of the base antenna grade on the performance of the rover stations. When the ANN–MS patch antenna was adopted at the base station, a metallic ground plane of 15 cm diameter was placed underneath to reduce multipath. The antenna of the base station was connected via a signal splitter (GPS source RMS18) to two GNSS receivers; a low-cost u-blox M8T GNSS receiver and a Leica GS10 receiver (Fig. 2A). The aim of different grades of GNSS base receiver was to assess their impact on the performance of rover stations.

Regarding the rover GNSS stations, they were mounted on the experimental device of circular motion (Fig. 2B). The circular motion device, which was mounted at pillar NGB3, consisted of two symmetrical metal arms, which can execute circular motion at a constant angular velocity (ω = 2.275 rad/s) and frequency. There were six screw threads on each arm at distances of 5 cm, 10 cm, 20 cm, 30 cm, 40 cm, and 50 cm from the circular motion centre (Fig. S1). On one arm, two low-cost GNSS receivers were deployed on a large ground plate for multipath mitigation, each connected to a patch antenna which is of the same model with the base patch antenna (i.e., ANN-MS). The two patch antennas were closely spaced (~20 cm) at the same designated rotation radius with the same orientation to azimuth. On the other arm, the geodetic rover station (Leica GS10-AS10) was deployed, with the antenna mounted on the same rotation radius. The executed circular motions with rotating radii between 10 and 50 cm were recorded simultaneously by both the geodetic and low-cost GNSS receivers. The executed circular motion of 5 cm was recorded only by the low-cost GNSS receivers due to the lack of space for the geodetic antenna installation.
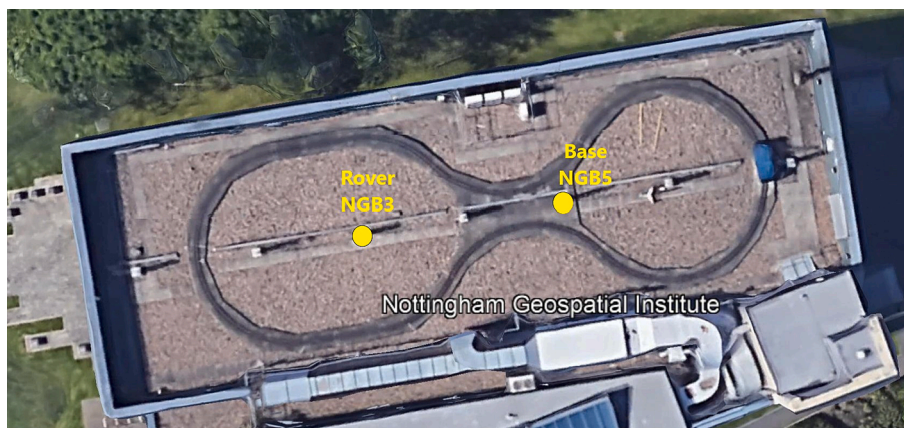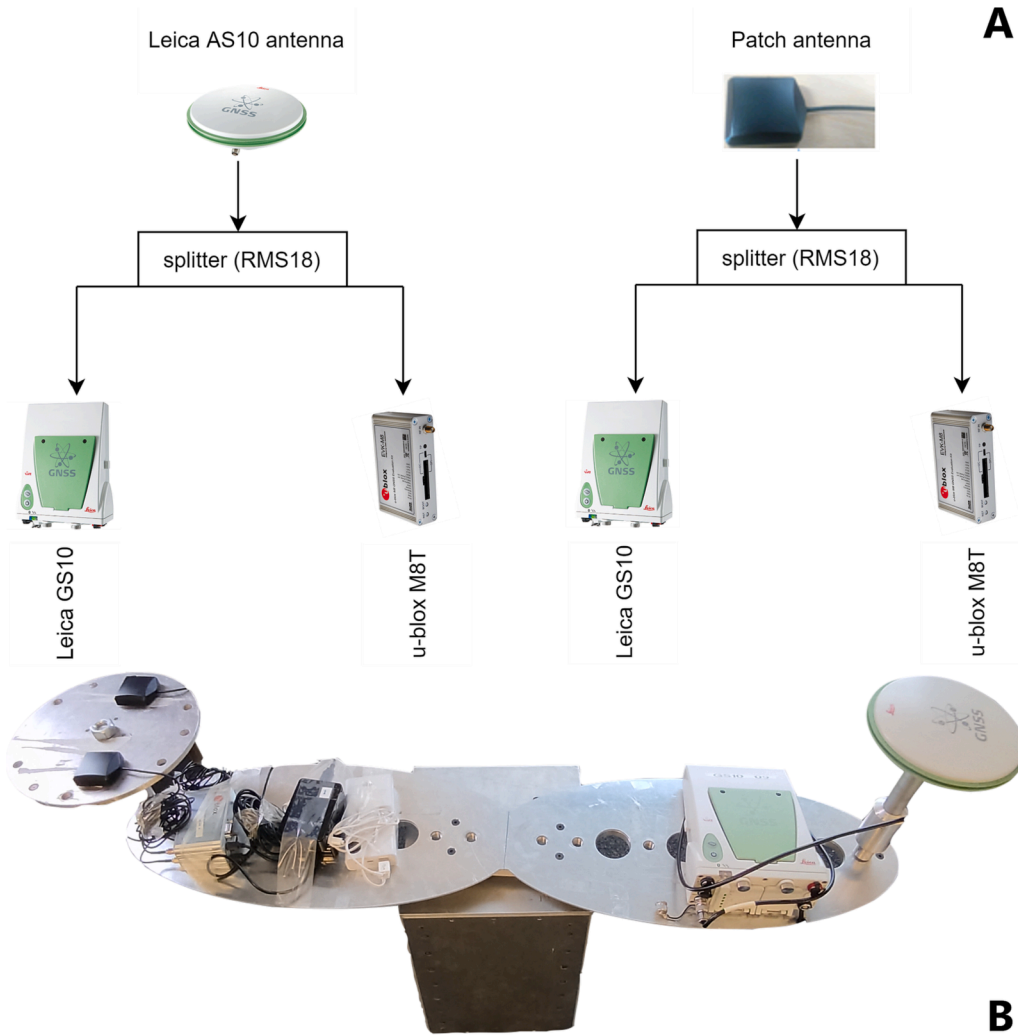

Fig. 1. Satellite view of the NGI roof with NGB5, and NGB3 control points, where the reference and rover stations (circular motion device) were installed.

A

Fig. 2. (A) Different base station configurations: the Leica AS10 and patch antenna are connected to the Leica GS10 and u-blox M8T receivers via a signal splitter. (B) The rotation motor, which could execute horizontal circular rotation, and two symmetrical blades on which the measuring equipment was deployed: On each blade, six screw threads were designed at distances of 5 cm, 10 cm, 20 cm, 30 cm, 40 cm, 50 cm to the rotation centre (Supplementary Fig. S1). In the current stage, the two u-blox rovers (patch antennas with the u-blox receivers) were installed on the left with two raspberry pi 3 data loggers and a power bank; the Leica GS10 receiver and AS10 antenna were installed on the right. Both installations were at a rotation radius of 50 cm.

B

Each circular motion experiment lasted 10–15 min in order to: (i) have duration similar (or even longer) to that of experiments of previous studies on examining GNSS in dynamic motion [35,36]; (ii) be consistent with the duration of time-intervals which are analysed in bridge monitoring application, which is about 10 min [6]; (iii) allow the motor to execute 200–300 full cycles of motion, with 10 Hz sampling frequency and 6000–9000 GNSS coordinate scatters, reasonable to define the circular trajectory and (iv) the GNSS data will still be affected by multipath errors. Actually, the latter led to splitting the time-period in smaller periods of 100 s to analyse more explicitly the GNSS data precision. The GNSS receivers recorded the trajectory of the executed circular motions with 10 Hz sampling rate, by collecting multi-GNSS observations, including GPS, Galileo and GLONASS satellites. The low-cost GNSS receiver's measurements were logged on Raspberry pi 3. It should be mentioned that u-blox M8T could only track maximum three constellations concurrently (either GPS + GLONASS + Galileo or GPS + Galileo + BeiDou) due to the dual-frequency radio frequency (RF) architecture [45], whereas, the dual frequency ZED-F9P modules are capable of tracking four GNSS constellations concurrently (GPS, GLONASS, Galileo and BeiDou) due to the multi-band RF front-end architecture [46], which could be useful for future studies.

4. GNSS data processing

Table 1 shows all the available short baseline combinations of GNSS base-rover stations processed for the circular motion experiments. There

Table 1
Cases of the baseline formations for the circular motion experiments.

Case	Base		Rover	
	Antenna	Receiver	Antenna	Receiver
I	Leica AS10	U-blox M8T	Patch	U-blox M8T
			Patch	U-blox M8T
			Leica AS10	Leica GS10
II	Leica AS10	Leica GS10	Patch	U-blox M8T
			Patch	U-blox M8T
			Leica AS10	Leica GS10
III	Patch	U-blox M8T	Patch	U-blox M8T
			Patch	U-blox M8T
			Leica AS10	Leica GS10
IV	Patch	Leica GS10	Patch	U-blox M8T
			Patch	U-blox M8T
			Leica AS10	Leica GS10

were four formations of the base GNSS station. On the other hand, there were three GNSS rover stations deployed on the circular motion device; two u-blox M8T GNSS receivers connected to the patch antenna and a Leica GS10 receiver connected to the Leica AS10 antenna. Any possible GNSS base-rover baseline formation was processed for any of the

examined rotation radii (from 5 cm to 50 cm); only the u-blox rover stations were used for the circular motion of 5 cm.

The GNSS data acquired was post-processed in kinematic mode (PPK). PPK is a GNSS technique frequently adopted in dynamic deformation monitoring applications [36,47]. To obtain the final baseline solution in a local E/N/U coordinate system, we followed the following step for the GNSS processing: firstly, the base and rover GNSS raw observation data were pre-processed and converted to Receiver Independent Exchange format (RINEX) files using 'TEQC' [48] and 'convbin' (RTKLIB CUI for RINEX conversion) [13] for Leica and u-blox raw data, respectively. Then, the base and rover RINEX data of different baseline cases (cases I-IV; Table 1) were post-processed in the 'RTKPOST' module in RTKLIB (version demo5 b33c [49]) for the coordinate computation of the corresponding rover receiver with respect the base station. Compared to the original in-built feature of RTKLIB, the adapted version (demo5 b33c) has a few improvements [50], one of which is to use additional adjustable constraints for integer ambiguity resolution (e.g., minimum number of satellites necessary to get a fix; or to hold an integer ambiguity). These constraints successfully mitigate the false fixes in the results processed by the original version of RTKLIB [13].

In the GNSS 'RTKPOST' post-processing step, the Extended Kalman Filtering (EKF) algorithm was applied, configured both in the forward and backward direction (defined as 'combined' option in the settings). The continuous integer ambiguity resolution was employed, with a 15-degree elevation mask in kinematic mode. The stochastic model employed to describe the variance of carrier-phase or pseudorange error is an a-priori elevation-dependent cosecant variance model with user-defined parameters [13], where we define the 'a' and 'b' parameter in 'carrier-phase error model function (a + b/sin(elevation))' as default value of both 0.003, respectively. For an efficient integer ambiguities estimation, the integer least square (ILS) problem was resolved adopting LAMBDA [51] and MLAMBDA [52] method, which is then combined and validated by the simple 'ratio-test' integer aperture estimator with a default ratio threshold value of 3 [13]. Additionally, broadcast ionospheric corrections and Saastomoinen tropospheric models were configured to account for the residual atmospheric errors. For single frequency measurement, the cycle slips are detected by loss of lock indicator (LLI) in the input RINEX measurements, and the single-difference carrier phase bias is reset to initial value on cycle slip detection [53].

The output of GNSS data processing was the baseline solution in a local Easting (E), Northing (N), and Up (U) coordinate system. For all baseline combinations, both GPS-only and GPS + Galileo GNSS data were processed. The GLONASS observations were not used in the processing due to their incompatibility with the u-blox receiver, which would lead to data loss [28]. On the other hand, the GLONASS associated inter-frequency bias (IFB) would present a problem [54] when different models of receivers are adopted in the rover and base [55].

5. GNSS time-series analysis

The circular motion device executed horizontal circular motion with constant frequency in the horizontal plane. Therefore, the GNSS *E/N* coordinates should have periodic variations of amplitude equal to the circular motion radius. In the *Up* component, no variation was expected; however, due to potential mis-levelling of the device, some periodic variations of the *Up* component could be expected.

To remove the potential outliers within the time-series, we firstly adopted the 3-σ criterion in order to mitigate the outlier impact on further analysis [36]. For each experiment and set of GNSS measurements, the circular motion was modelled by defining the optimum circle and determining the respective radius and the Easting/Northing trajectories. The assessment of the performance of the low-cost GNSS receiver was based on: (i) the standard deviation of the radius residual and (ii) the standard deviation of *E/N* residuals.

The radius of the optimum circle was computed based on the Pratt

method [56] using least–squares fitting [57]. Then, the radius residuals for each experiment of GNSS measurements were calculated using Equation (1):

$$\text{Radius residual} = D - R \tag{1}$$

where D = the distance from (E, N) measurement of each epoch to the estimated centre of the fitted model, R = the radius of the best-fit circle.

To define the optimal sinusoidal model of *E/N* coordinates, the model designed by Seibold [58] was applied, which is suitable for the sine-curve fitting of noisy time-series. The parameters for modelling the sinusoidal equations were estimated by Fast Fourier transform (FFT) and nonlinear fitting, where the frequency, amplitude, and phase of the largest FFT peak were used as initial values for the regression analysis. Based on the sinusoidal model for each experiment, the *E/N* residuals were computed. To limit potential non-linearities in the function of the circular device, the period of 10-minute length of each experiment was split into six 100-second intervals for the modelling of the sinusoidal models and the calculation of the residuals. This was necessary since the GNSS measurements would drift quickly from the sinusoidal model if a longer period of datasets (e.g., 600 s) were analysed, making it infeasible to be modelled by a global sinusoidal model of uniform frequency, probably due to the nuances in the oscillation frequency (angular velocity) between different time windows.

The analysis of the radius and *E/N* residuals was conducted for the various radii of circular motion, satellite constellation and type of base receivers to assess their impact on the accuracy of the low-cost receivers. Furthermore, the residual time-series were also used to assess the potential improvement of the low-cost GNSS receiver's performance by applying the three strategies (high-pass filtering, average and CME).

Finally, spectral analysis was also carried out for all the GNSS time-series of various rotation amplitudes, multi-constellations, and different rover-base baseline combinations to estimate the dominant frequency of the circular motion and assess whether any of the GNSS parameters (i.e., amplitude, constellation, type of base receiver) have an impact on the accuracy of the frequency estimation.

6. Short-baseline experiment results

The u-blox (with patch antenna) GPS + Galileo (G + E) solution of case II (base station with Leica AS10-GS10) for 20 cm circular motion is analysed as a representative experiment for GNSS time-series analysis. Fig. 3 illustrates the E-N planar trajectory of GNSS measurements and the fitted circular model by the Pratt method. The *E/N/U* time-series and Discrete Fourier Transform (DFT) spectral analysis are presented in
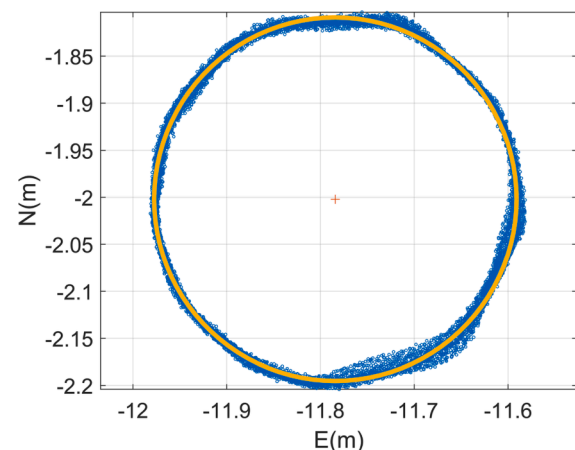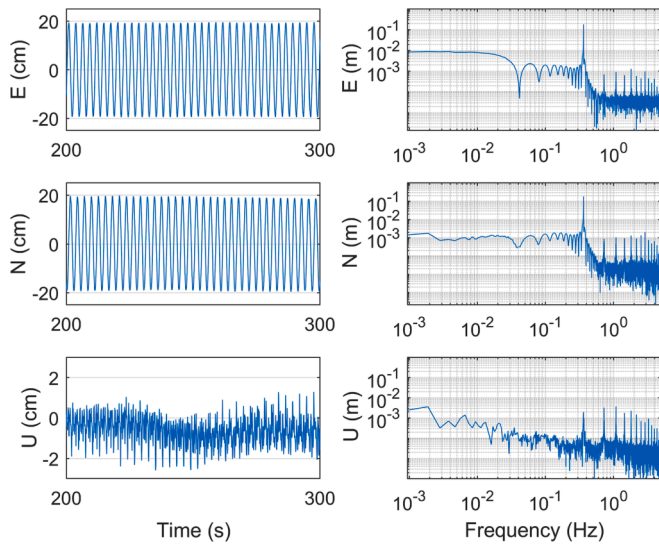

Fig. 3. Scatterplot of Northings versus Eastings of the u-blox 1 with patch antenna G + E solution in case II for ~20 cm rotation radius, and the fitted circle using Pratt method (orange).

Fig. 4. (Left) E/N/U time-series of a 100-second duration extracted from the whole ~15 min time-series after shifting to near-zero value, showing oscillation motion in E/N direction, and noise in Up direction (E/N shift based on the centre of the circle, U shifts based on the mean-average of U coordinate); **(Right)** DFT spectra of the corresponding E/N/U components based on the ~15 min duration.

Fig. 4. The vertical axis *E/N* time-series is shifted to oscillate around zero by configuring the centre of the best-fit circle as the origin. For the *Up* time-series, the mean-average is subtracted from the initial time-series to examine the coordinate variation in the *Up* direction.

The time-series in *E/N* direction express a periodic pattern of sinusoidal oscillation with an amplitude of ~20 cm, and the *Up* time-series express mainly GNSS measurement noise. In the DFT spectra of the *E/N/U* time-series, the dominant frequency of all the components is 0.362 Hz, agreeing with the circular motion frequency. However, other peaks are also detected in integer multiples of 0.362 Hz, which are probably due to the motor harmonics. The harmonics inevitably occur in rotation machines due to the imperfect sinusoidal distributed windings slots, which generate distorted magnetomotive forces (MMF) and eventually lead to harmonics [59]. It should be noted that the same dominant frequency and the harmonics were also observed in the spectra of the Leica GNSS measurements. A similar phenomenon was observed in the spectra of low-cost GNSS measurements in the study by Jo et al. [16], which, however, was attributed to GNSS measurements quantisation error.

Based on the fitted circle and the sinusoidal waveform model, using the Pratt model and Seibold method respectively, the residual time-series of the radius and of the *E/N* GNSS time–series were computed. Fig. 5 shows the time-series and spectrum of radius residuals. The radius residuals vary with time in a zone of ±1 cm. A frequency of ~0.36 Hz is still detected without being dominant. Fig. 6 shows the *E/N/U* residual
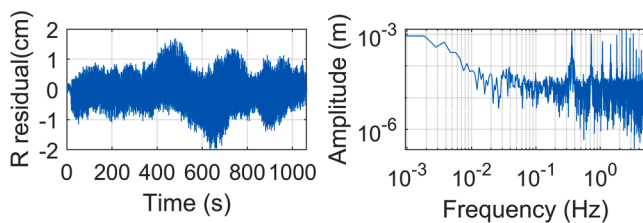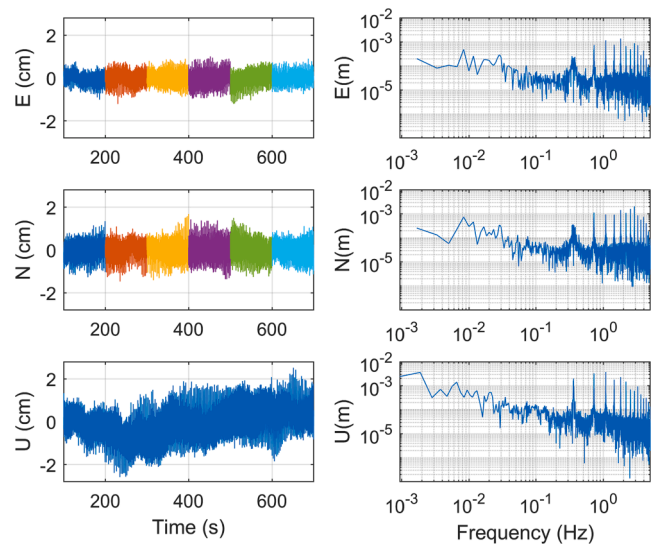
Fig. 6. (Left) E/N/U residual time-series for G + E solutions with u-blox 1 receiver with patch antenna as the rover and Leica receiver with AS10 antenna as the base for ~20 cm rotation radius, **(Right)** corresponding DFT spectra of E/N/U residual time-series.
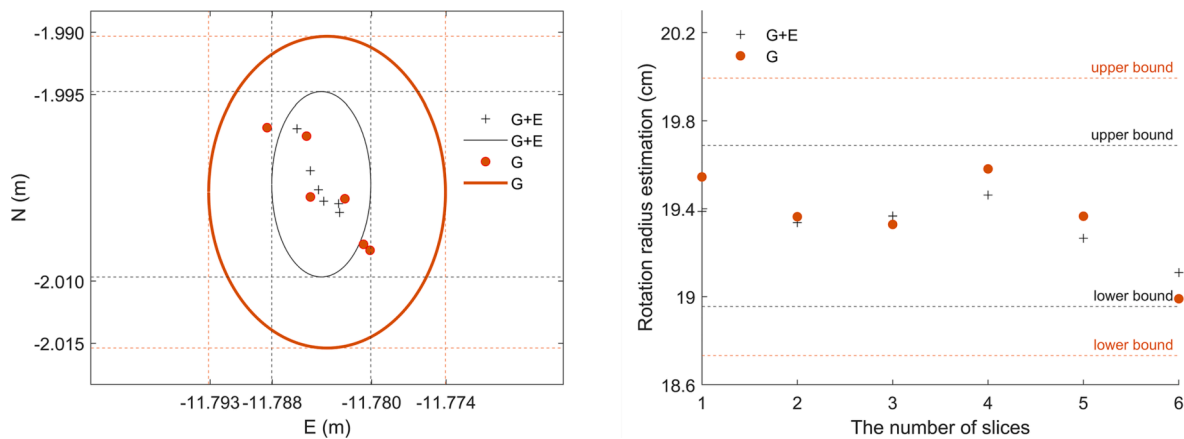
time-series and the corresponding spectra. Similar to the spectrum of radius residual, the spectra of *E/N* residual also reveal a frequency around 0.33–0.38 Hz after removing the sinusoidal pattern of the circular motion and the corresponding harmonics can still be detected, with frequency peaks higher than the frequency of the circular motion or the low-frequency noise. The existence of the initial harmonic frequencies even after filtering of the dominant frequency is an indication that these frequencies are not due to the aliasing effect [39]. To examine the consistency of the six intervals of 100-second data, Fig. 7 is plotted. It is shown with GPS + Galileo constellation, higher consistency is detected compared to GPS-only result, either from bounding ellipses (acceptance areas) constructed from 3-σ rejection criterion based on the rotation centre coordinate estimations [36] or the 3-σ upper/lower bounds of the radius estimation. Table 2 also shows a high consistency between analysis of six individual intervals. Based on 3-σ criterion, the centre coordinates are generally bounded within up to ±0.01 m acceptance area and the estimated radii are within ±0.006 m.

7. Precision of the radius and *E/N/U* measurement

The analysis presented in section 6 was applied in all cases of (i) different rotation amplitudes, (ii) different rover-base baseline combinations, and (iii) GPS only and GPS + Galileo solutions. Moreover, the parameters to represent measurement precisions were evaluated and summarised for each case.

The radius (*R*) and the *E/N/U* residuals time-series were analysed to define the corresponding precision for the cases I to IV for different GNSS receivers for rover stations (u-blox 1, u-blox 3, and Leica) and summarised in Table 3, Table 4, and supplementary material (Tables S1, S2, S3, S4, S5, S6). From the *R* and *E/N/U* residuals time-series analysis, it is obvious that the base station receiver grade (u-blox or Leica receiver) has trivial impact on the precision of the GNSS time-series (Table 3). This is clearly reflected in the minor differences between GNSS time–series of different grades of GNSS base receivers, having a standard deviation of ~0.5 mm, ~0.7 mm, and ~1 mm for *E, N, U* components, respectively, regardless of the base antenna adopted (Fig. 8). The observation is also made for cases when the other u-blox rover and Leica rover were adopted, for different rotation amplitudes and multi-GNSS solutions accordingly, implying a trivial impact of base station receiver grade on the baseline time-series.

Furthermore, from *R* precision analysis of cases I and II (Fig. 9,

Fig. 5. (Left) R residual time-series for GPS + Galileo solution of ~20 cm rotation radius when the rover consisted of u-blox 1 and patch antenna, and base consisted of Leica receiver & AS10 antenna, **(Right)** corresponding DFT spectrum.

Fig. 7. **(Left)** The estimated rotation centre variation based on the results from six successive intervals of GPS only (G) and GPS + Galileo (G + E) time-series for ~20 cm rotation radius test when the rover adopts u-blox 1 & patch antenna and base adopts Leica GS10 & AS10 antenna, the respective ellipses for G and G + E were also created bounding the rotation centre based on 3-σ criterion, **(Right)** The corresponding estimated rotation radius variation, with upper bound and lower bound determined based on 3-σ criterion.

Table 2
The estimated Easting (X)/ Northing (Y) coordinates of the rotation centre and radii using 3-σ criterion (μ ± 3σ) based on the results of six successive intervals of the baseline time-series for case II when u-blox 1 and patch antenna rover was adopted (unit: m).

R (cm)	Centre Easting (X)		Centre Northing (Y)		Estimated R	
	GPS	GPS + Galileo	GPS	GPS + Galileo	GPS	GPS + Galileo
5	−11.782 ± 0.005	−11.782 ± 0.004	−2.004 ± 0.010	−2.002 ± 0.010	0.047 ± 0.005	0.047 ± 0.003
10	−11.777 ± 0.010	−11.780 ± 0.005	−1.997 ± 0.010	−2.000 ± 0.005	0.104 ± 0.003	0.102 ± 0.002
20	−11.784 ± 0.010	−11.784 ± 0.004	−2.003 ± 0.013	−2.002 ± 0.008	0.194 ± 0.006	0.193 ± 0.004
30	−11.781 ± 0.005	−11.782 ± 0.003	−2.002 ± 0.006	−2.002 ± 0.004	0.308 ± 0.002	0.307 ± 0.002
40	−11.782 ± 0.003	−11.782 ± 0.001	−2.004 ± 0.006	−2.002 ± 0.004	0.402 ± 0.002	0.402 ± 0.000
50	−11.781 ± 0.003	−11.782 ± 0.003	−1.998 ± 0.008	−2.003 ± 0.009	0.502 ± 0.003	0.502 ± 0.002

Tables 3, S1, S2), it is confirmed that higher precision can be achieved with Leica receiver as rover than u-blox rover regarding the same rotation amplitude for both GPS and GPS + Galileo solutions. However, the incorporation of the Galileo system to GPS enhances the precision of the GNSS solution, especially for the low-cost GNSS receiver. The precision of Leica and u-blox GPS-only solutions regarding the ~20 cm and ~50 cm radii tests are significantly poorer than those derived from other rotation amplitudes, indicating a potential weaker GPS geometry. However, the precision difference between different amplitudes was minimised with GPS + Galileo solutions. Similar conclusions are also drawn from the solutions for case III and case IV when the patch antenna is used in the base (Fig. 9 and Tables S3, S4, S5). Whereas it is noticed that the standard deviation of *R* residuals for the ~20 cm rotation test is significantly higher for u-blox 3 due to mishandling of the equipment leading to the unstable deployment of the receiver (Fig. 9). It is also noticed that compared to other rotation amplitudes, an overall relatively lower precision was detected for ~10 cm amplitude from u-blox rovers (Fig. 9). This is probably due to the GNSS signals transmitted to the

patch antenna were interfered by the closely-mounted geodetic antenna.

The base station antenna impact on *R* precision is also investigated in Fig. 9, where it is evident that the beneficial impact of the geodetic-grade base antenna (Leica AS10) on the precision of *R* measurement, compared with that of the low-cost base antenna. For instance, improvement up to 2.5 mm for GPS + Galileo solutions is achieved by adopting a geodetic–grade base antenna when u-blox 1 is used as the rover (rotation radius ~20 cm). It is generally shown that when the AS10 antenna is used at the base station for GPS + Galileo solutions, the precision of the radius of the Leica GNSS rover station is about 2–3 mm, whereas it is about 3–7 mm for the low-cost GNSS rover station. On the other hand, when the patch antenna is used at the base station, the precision of radius of the Leica and low-cost GNSS rover measurement is about 3 mm and 4–8 mm, respectively.

The standard deviations of *E/N/U* residuals for cases I to IV are summarised in Tables 4 and S6, respectively. Firstly, it should be observed that the *E* component has higher precision than the *N* component due to the *E-W* baseline orientation, which affects the DD GNSS solution [28]. The precision achieved for different grades of base receivers is similar (i.e., case I&II or case III&IV). Therefore, only case II (Table 4) and case IV (Table S6) are presented and illustrated in Figs. 10 and 11. It is generally observed again that the Leica receiver has higher precision than the u-blox receivers, but the precision of the low-cost receivers is significantly improved with the GPS + Galileo solution. For instance, the precision of the *N* component of u-blox 1 is improved from 7.3 mm for GPS-only solution to 4.4 mm for GPS + Galileo solution, while the precision of Leica receiver for GPS + Galileo solution for the same test (*R* = 20 cm) is 2.7 mm.

The effect of the different base antennas on the *E/N* measurement precision is illustrated in Fig. 11. It can be observed that regardless of the rover station, the *E/N* measurement results adopting Leica AS10 base

Table 3
Standard deviation (in mm) of radius residuals for various rotation radius (in cm) based on GPS and GPS + Galileo solution for cases I and II when u-blox 1 and patch antenna was used in the rover.

| Unit (cm)	Case I U-blox 1 rover		Case II U-blox 1 rover	
Rotation Radius	GPS	GPS + Galileo	GPS	GPS + Galileo
5	4.8	4.4	4.8	4.4
10	7.5	5.8	7.5	5.8
20	8.1	4.4	8.0	4.4
30	4.3	3.3	4.3	3.3
40	3.8	3.2	3.8	3.1
50	6.7	4.3	6.7	4.3

Table 4
E/N/U residuals standard deviation (mm) of various rotation amplitude (5 cm-50 cm) based on GPS and GPS + Galileo baseline solutions formed by respective Leica, u-blox 1, u-blox 3 rover for case II.

R (cm)	Leica						U-blox 1						U-blox 3					
	G			G + E			G			G + E			G			G + E		
	E	N	U	E	N	U	E	N	U	E	N	U	E	N	U	E	N	U
5							2.4	4.4	6.0	2.1	4.0	5.7	4.9	6.8	7.8	3.4	5.8	8.1
10	1.8	3.4	3.4	1.3	2.5	2.5	4.6	9.4	12.2	3.7	7.0	11.0	4.9	13.0	14.4	3.7	9.1	9.0
20	3.1	4.4	4.3	1.7	2.7	2.4	5.4	7.3	9.3	3.2	4.4	6.5	4.6	7.5	10.2	3.1	4.8	6.6
30	2.2	2.8	4.0	1.8	2.2	3.4	3.1	4.8	6.4	2.4	4.0	4.7	3.2	4.6	4.9	2.8	4.6	4.7
40	2.2	3.1	3.8	1.8	2.5	3.1	2.8	4.2	6.9	2.5	3.3	5.5	2.7	4.7	6.8	2.4	4.4	4.7
50	2.8	4.3	5.3	2.5	2.9	3.0	4.3	9.3	19.1	3.3	4.6	7.9	3.6	9.3	12.3	2.9	4.6	6.3
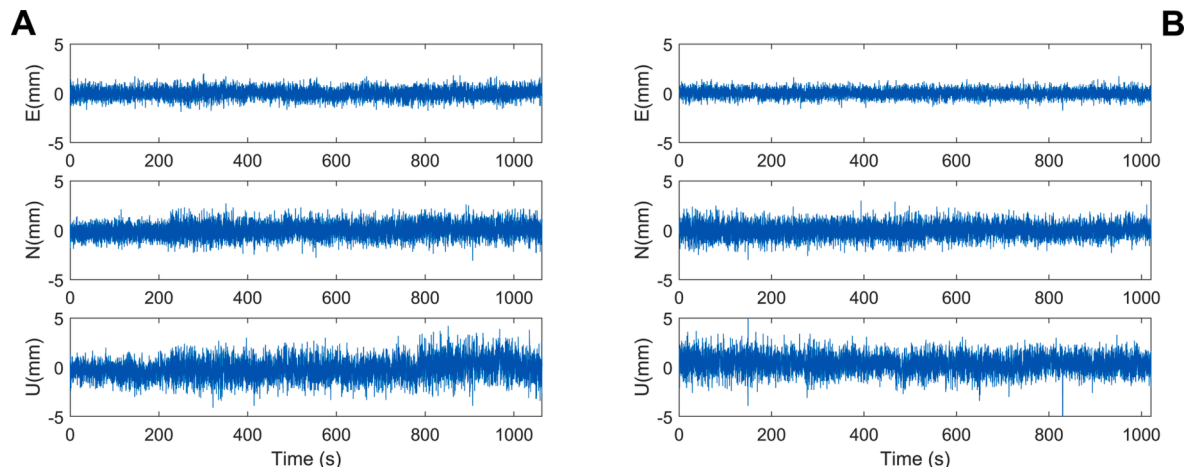
Fig. 8. A: The difference between the E/N/U GPS only time-series for the ~20 cm rotation radius test of the baselines formed by (i) rover: U-blox 1 - patch antenna and base: Leica GS10 - AS10 and (ii) rover: U-blox 1 - patch antenna and base: u-blox - AS10. **B:** The difference between the E/N/U GPS only time-series for the ~20 cm rotation radius test of the baseline formed of (iii) rover: U-blox 1 - patch antenna and base: Leica GS10 - patch antenna and (iv) rover: U-blox 1 - patch antenna and base: u-blox - patch antenna.
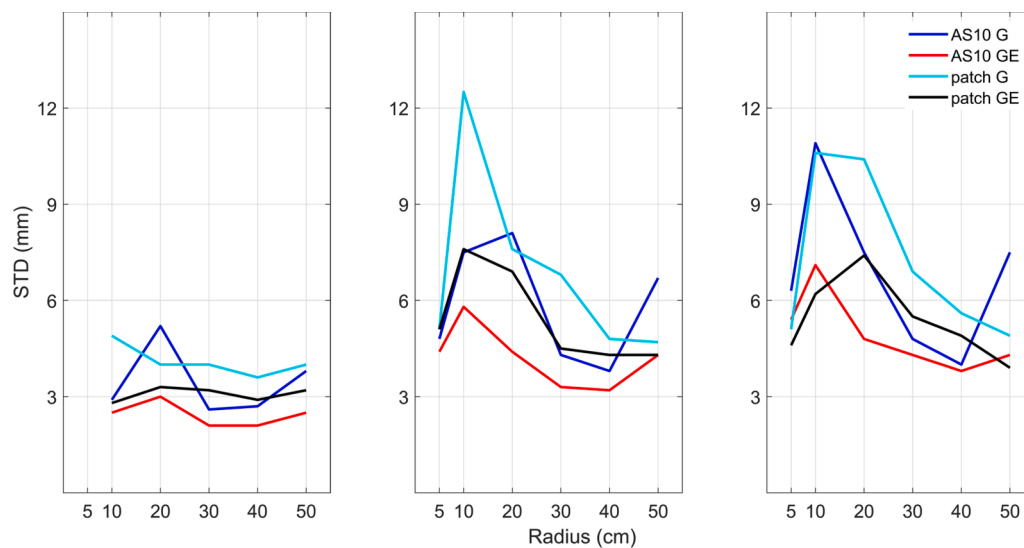

Fig. 9. Standard deviation of R residuals of **(Left)** Leica rover, **(Middle)** u-blox 1, and **(Right)** u-blox 3, for the base station consisted of Leica GS10 receiver and AS10/patch antenna for GPS-only (G) and GPS + Galileo (GE) solutions.

antenna are generally more precise than that with patch base antenna, which is clearly represented by u-blox 1/u-blox 3 GPS + Galileo *N*-component. For instance, the precision of the *N*-component of GPS + Galileo solution for the 20 cm rotation radius is 7.1 mm for the patch antenna at the base station. However, the precision is improved significantly when the AS10 antenna is used in the base, reaching 4.4 mm. The Easting precision improvement is also generally improved by adopting a geodetic antenna at the base but in order of less than 1 mm.
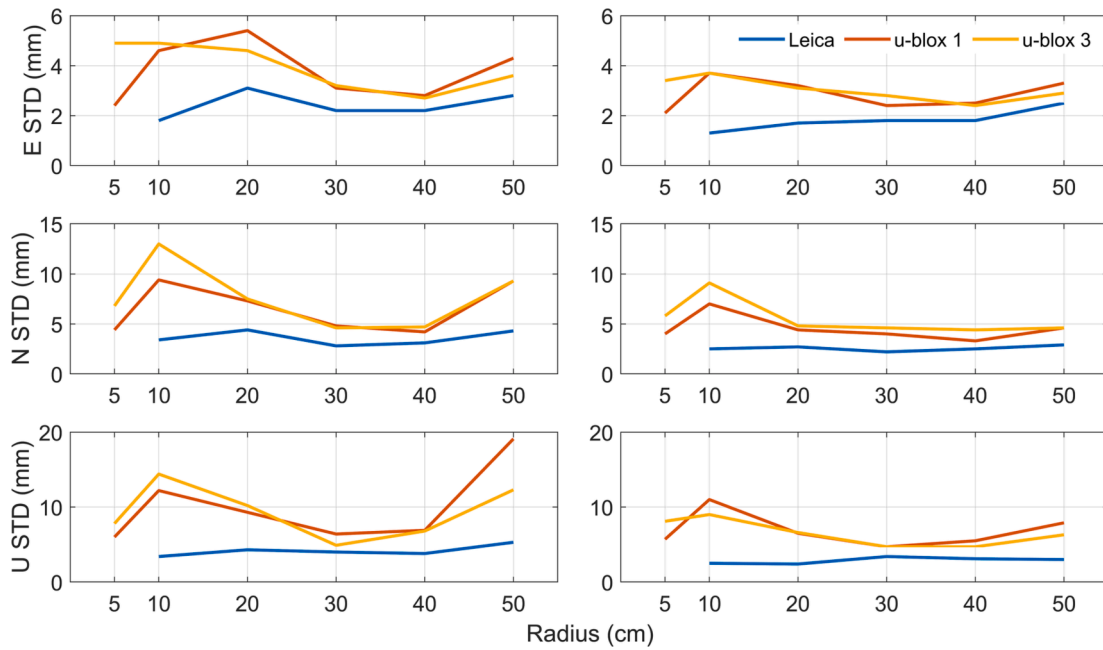
Fig. 10. E/N/U residual standard deviation for different rotation amplitudes based on **(Left)** GPS (G) and **(Right)** GPS + Galileo (G + E) baseline solutions formed by Leica, u-blox 1, and u-blox 3 rover and Leica GS10/AS10 base (standard deviation calculated based on 10-min oscillation period).
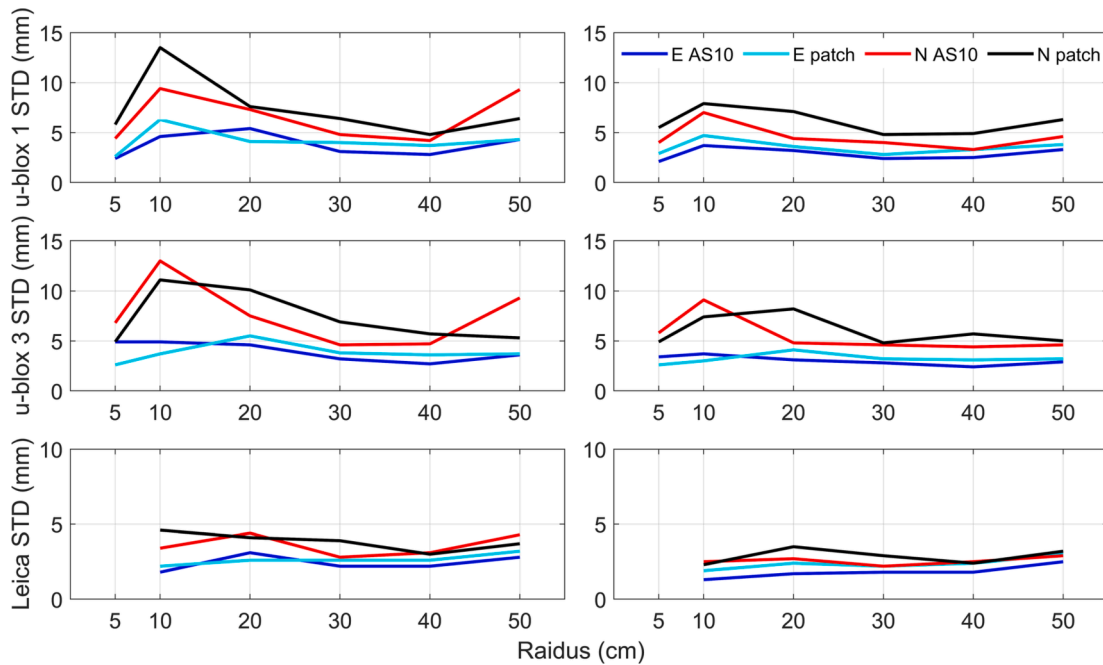
Fig. 11. E/N residual time-series standard deviation of baseline formed by rover (u-blox 1, u-blox 3, Leica) and base (Leica GS10 & patch antenna/ Leica GS10& AS10), **(Left)** GPS only solution; **(Right)** GPS + Galileo solution. (standard deviation calculated based on 10 min oscillation period) E patch & N patch stand for the standard deviation of Easting, Northing residual with patch antenna as base antenna respectively. E AS10 & N AS10 stand for the standard deviation of Easting, Northing residual with Leica AS10 antenna as base antenna, respectively.

8. Precision improvement by a dual low-cost receiver solution

To explore the possibility of precision enhancement, three strategies were attempted on the baseline time-series obtained using PPK technique, (1) average combination, (2) CME filter, and (3) high-pass filter. The first two strategies were applied by combining the solutions of the two closely-spaced low-cost GNSS receivers, while the high-pass filter strategy could be applied independently to each receiver and the average combined solution.

More specifically, in the average combination strategy, the initial time-series of the two low–cost GNSS receivers solutions were averaged since they share common pattern of displacement, aiming to limit potential errors of the receivers [16]. This is implemented by using Eq. (2):

$$x_{ave}{}^i = \frac{X_{u-blox1}{}^i + X_{u-blox3}{}^i}{2} \tag{2}$$

where × represents the time-series component (i.e., N/E/U), the subscripts denote the average, u-blox 1, and u-blox 3 cases respectively, and

the superscript denotes the same current i^{th} epoch which constructs the time-series.

In the CME strategy, the two u-blox $E/N/U$ initial time-series were firstly analysed by using a low-pass filter (i.e., 8th order Chebyshev with a cut-off frequency of 0.1 Hz) to extract the low–frequency noise within the time-series. Then cross-correlation analysis was conducted between the low-pass filtered time-series of the two low-cost GNSS receivers. In the case of a high correlation of the low-frequency time-series (Table S7), the common low-frequency noise of the two GNSS receivers was modelled with the CME modelling formula (Eq. (3)):

$$CME_t = \frac{\frac{R_t^i}{(\sigma_t^i)^2} + \frac{R_t^j}{(\sigma_t^j)^2}}{\frac{1}{(\sigma_t^i)^2} + \frac{1}{(\sigma_t^j)^2}} \tag{3}$$

where CME_t is the common-mode error between station i and j at time t, R_t^i and R_t^j are the coordinate residuals for station i at time t, where in this context, the low-pass filtered time–series is used to represent low-frequency errors, σ_t^i and σ_t^j are the respective standard deviation estimates for the solution point for station i and j at time t which could be directly derived from RTKLIB output.

The CME model was then applied to filter the two low-cost GNSS time-series, and the derived filtered time-series were averaged to further reduce potential noise. Fig. 12 shows a representative example of the CME strategy for the experiment of radius 20 cm, where the u–blox 1 and u-blox 3 low-pass filtered $E/N/U$ time-series are presented. The CME model was produced based on the low-pass filtered time-series of u-blox 1 and u-blox 3 and then subtracted separately from the initial u-blox 1 and u-blox 3 time-series. Finally, the two filtered (u-blox 1 and u-blox 3) times-series were averaged. It can be seen on the left panel in Fig. 12 that compared to the Up time-series, a lower amplitude of the low-frequency component is detected in E/N, which might suggest multipath's less influence on the horizontal plane than in the vertical direction due to planar rotation of the motor. On the middle and right panel, the separate and combined low-cost GNSS time-series (averaged results after CME filter) were compared to examine the impact of the CME filtering and averaging strategy on the time-series. It is demonstrated that the precision improvement from CME filter could not be directly identified

from the E/N time-series. However, based on the Up components, it is shown that the combined time-series is more accurate as the Up components should be constant and are expected to steadily oscillate around zero.

For the high-pass filter, Chebyshev high-pass filters of 8th order, passband frequency of 0.1 Hz, and passband ripple of 1 dB were applied to u-blox 1, u-blox 3 $E/N/U$ time-series in order to attenuate signals below the cut-off frequency, which is contaminated by low-frequency errors. The Chebyshev type I high-pass filter was selected due to its steeper roll-off with comparatively lower passband ripple, which is adopted in many literature to mitigate the GNSS multipath biases [60,61,62]. The cut-off frequency of 0.1 Hz was adopted by the high-pass and low-pass aforementioned, since most low-frequency errors including multipath correspond to frequency band lower than 0.1 Hz [63,64,65]. Furthermore, the main modal frequencies of flexible structures are usually higher than 0.1 Hz, which is why cut-off frequency of 0.1 Hz has been applied in high-pass filterers of GNSS structural monitoring studies [3,7,62]. The u-blox 1 and u-blox 3 high-pass filtered time-series were then averaged to limit the potential impact of the high-frequency noise of the two receivers.

Firstly, it is examined whether the average combination of the initial u-blox time-series would improve the measured precision. Using a similar analytical approach, the $E/N/U$ precisions of (i) the separate u-blox and average combined initial time-series, (ii) the time-series after CME filtering, and (iii) the time-series after high-pass filtering were analysed for Leica AS10 base antenna and patch base antenna, respectively. Based on the results, Fig. 13 is plotted to compare the precision improvement for the different strategies.

It is shown the average combination of the two u-blox time-series would generally improve the precision of the results irrespective of whether it is applied to the initial time-series, used together with the CME filter, or high-pass filter (Fig. 13). For example, compared to the u–blox 1 only solution, the precision of the average combined GNSS time-series is improved from 4.3 mm to 2.4 mm in the Easting component for the initial GNSS time-series of 10 cm rotation radius test (Fig. 13), which probably limits the impact of the interference caused by AS10 antenna in the low-cost GNSS measurements, as mentioned in section 7. Regarding the CME filtered or the high-pass filtered GNSS
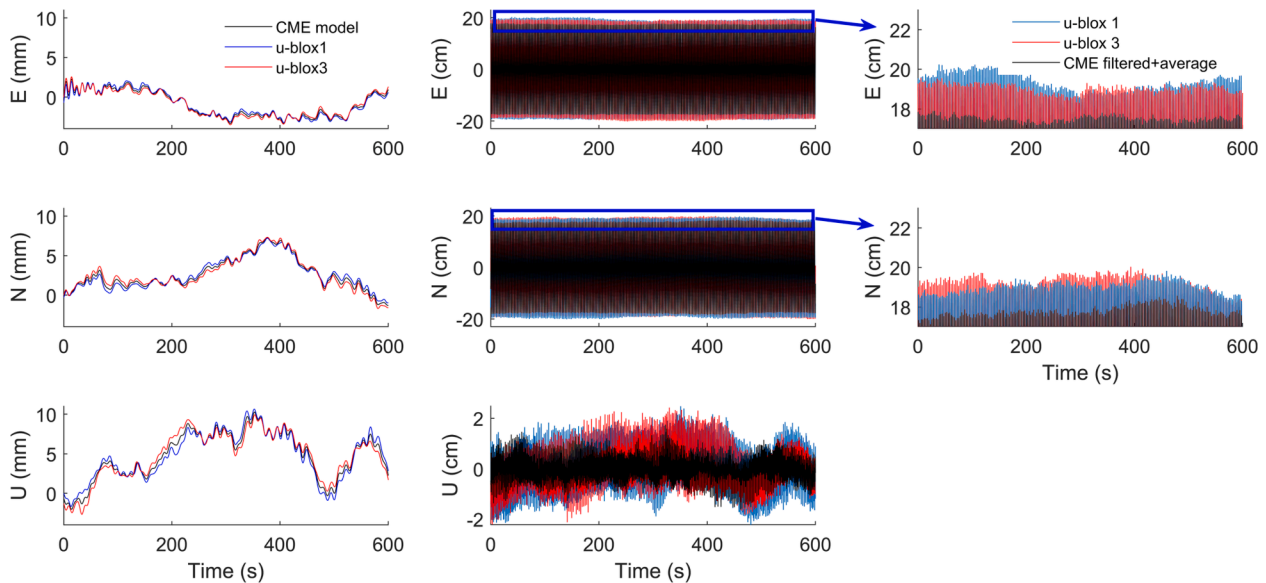
Fig. 12. (Left) Low-pass filtered E/N/U time-series for u-blox 1 and u-blox 3, and the low-frequency common mode error (CME) model. The initial E/N/U time-series is based on GPS + Galileo solutions for the ~20 cm rotation radius with the rover station consisted of u-blox 1 and patch antenna and base station consisted of Leica GS10 and AS10. **(Middle)** Initial E/N/U GNSS time-series of u-blox 1 and u-blox 3 receivers and the E/N/U GNSS combined time-series (i.e., after applying the CME filter and averaging the derived time-series). **(Right)** Zooming in the peak of E/N time-series of u-blox 1, u-blox 3 and the combined time-series (y-scale values around 20 cm) to demonstrate clearly the difference between the combined and the initial time-series.
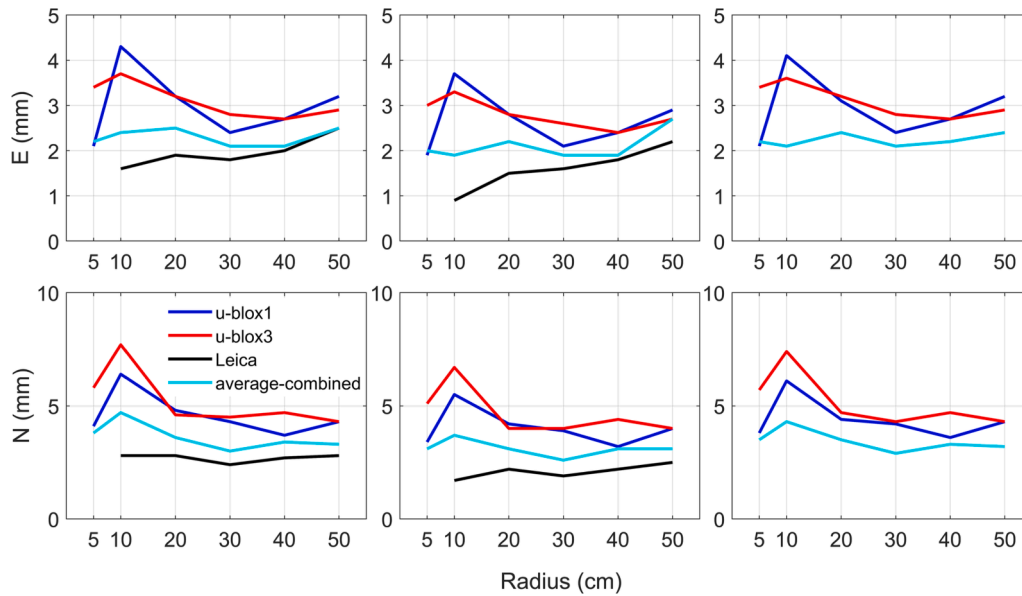
Fig. 13. Standard deviation of E/N from the **(Left)** original time-series, **(Middle)** high-pass filtered time-series, and **(Right)** CME filtered time-series of the u-blox 1, u-blox 3, average-combined, and Leica GPS + Galileo solutions for different rotation radii when the base station consisted of Leica GS10 and AS10 antenna.

time-series, it is shown that there is a clear precision improvement with respect to that of the initial GNSS time-series and generally a small improvement with respect to the averaged time-series of u-blox 1 and u-blox 3. For instance, for the case of Northing component of 10 cm radius, the high-pass filtering strategy enhances the precision by 1 mm, while the CME strategy results to lower precision improvement of up to 0.4 mm with respect to the averaged GNSS time-series.

An additional parameter to evaluate the impact of the three strategies on the precision of the low-cost GNSS receiver is the computation of the ratio of the standard deviation of the low–cost GNSS receiver for each strategy with respect to the standard deviation of the Leica receiver, as is expressed in Eq. (4):

$$Ratio = \frac{Precision^*}{Precision \ of \ Leica} \qquad (4)$$

where Precision of Leica = the E/N/U residual standard deviation from the initial Leica time-series.Precision* =the respective E/N/U residual

standard deviation from the initial, CME filtered or high-pass filtered result from u-blox, average combined u-blox, or Leica solutions.

In Fig. 14, it is presented the ratio of the E/N components of u-blox 1 and u-blox 3 receivers and how it varies depending on the adopted strategy (averaging, CME, high-pass filtering). It is shown that the standard deviations from the initial individual u-blox time-series are about one to three times of that from the Leica reference. However, the precision enhances with average combination, reaching a comparable level to the Leica results, with the ratio ranging between 1.00 and 1.68. Additionally, a decrease in the ratio from the initial time-series are also shown clearly if different filtering strategies are applied. For example, the ratio of the initial averaged time-series to the Leica reference is 1.50 for Easting component of the 10 cm rotation radius test, this ratio reduces to 1.31 for the CME filtered case and further reduces to 1.19 for the high-pass filtered case. Similar phenomena are also identified from other amplitude cases, Nothing component and with respect to u-blox 1 and u-blox 3 results. In general, it can be summarised that with low-cost
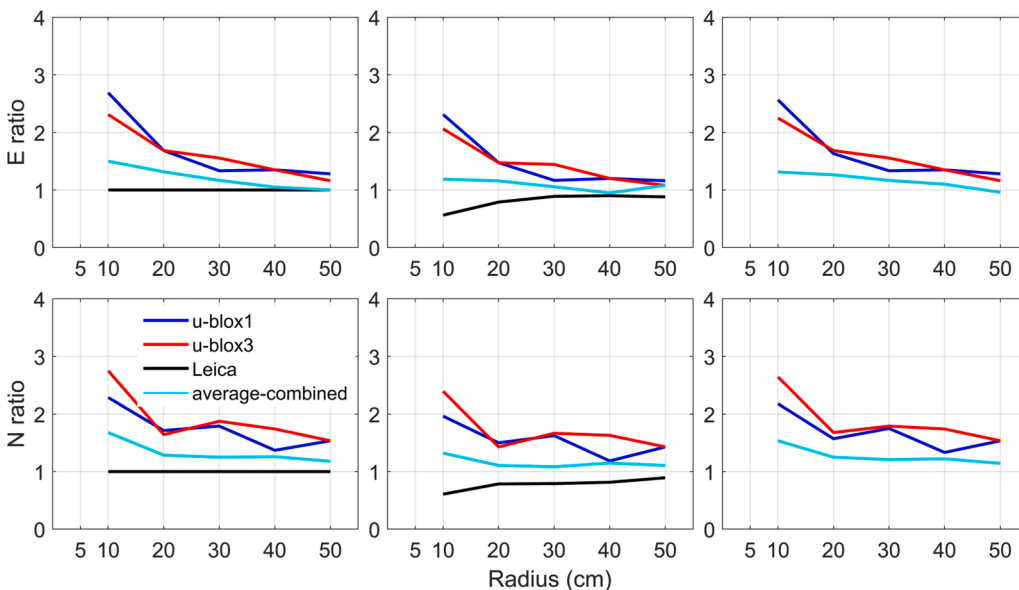
Fig. 14. E/N precision expressed as ratios with reference to the precision of original Leica results (ratio >1 implies precision degradation and ratio <1 indicates precision improvement) **(Left)** Original time-series, **(Middle)** high-pass filtered time-series, and **(Right)** CME filtered time-series of the u-blox 1, u-blox 3, average-combined, and Leica GPS + Galileo solutions for different rotation radii when the base station consisted of Leica GS10 and AS10 antenna. The ratio when the rotation radius is 5 cm is not shown due to no Leica reference data.

Table 5
Precision of R estimation, derived as the mean value, μ, of the standard deviation and the 95% confidence level ($\pm 2\sigma_{\bar{x}}$) from all tests of different rotation radii, based on GPS only and GPS + Galileo solutions.

Base antenna	Rover station	The precision of R estimation (mm) ($\mu \pm 2\sigma_{\bar{x}}$)	
		GPS-only	GPS + Galileo
AS10	Leica	3.4 ± 0.9	2.4 ± 0.3
	U-blox 1	5.9 ± 1.3	4.2 ± 0.7
	U-blox 3	6.8 ± 1.8	5.0 ± 0.9
Patch	Leica	4.1 ± 0.4	3.1 ± 0.2
	U-blox 1	6.9 ± 2.2	5.5 ± 1.1
	U-blox 3	7.3 ± 1.9	5.4 ± 0.9

GNSS measurements, the largest enhancement is achieved by the high-pass filtered averaged solution, with the ratio ranging between 1.00 and 1.32. However, it is shown that by high-pass filtering of the initial Leica time–series, an even better precision could be attained than the initial Leica results with a ratio below 1 (Fig. 14 middle panel).

9. Discussion

From all GNSS time-series and spectral analyses of the short baseline dynamic motion test regarding different scenarios, it is confirmed from the spectral analyses of both low-cost and geodetic *E/N/U* GNSS (GPS only & GPS + Galileo) time-series that similar dominant frequencies at around 0.361–0.362 Hz could be retrieved for different oscillation amplitude ranging from 5 cm to 50 cm, which corresponds to the designated motor frequency with rotation angular velocity of 2.275 rad/s. On the other hand, from the time-series and measurement precision analyses, it is demonstrated that the base station receiver has a negligible impact on the *E/N/U* baseline coordinate time-series, since the standard deviation of differences between time-series adopting different base receivers is less than 1 mm. This leads to negligible differences in the derived measurement precision.

The precision of the different GNSS times-series, expressed as standard deviation, is compared between each case of time-series to evaluate the impact of different configurations on the results: (i) u-blox rover and Leica rover, (ii) GPS only and GPS + Galileo, (iii) geodetic base station antenna and patch base station antenna. By assuming the normal distribution of the residuals [36] and according to central limit theorem, Table 5 concludes the mean value (μ) of the precision (i.e., standard deviation) of *R* residuals and the respective range, expressed as the 95% confidence level ($\pm 2\sigma_{\bar{x}}$) (where $\sigma_{\bar{x}}$ is the standard error of the mean), summarised from tests with different rotation amplitudes to examine the influence of different configurations. Firstly, it is confirmed that the Leica rover has better precision (i.e., μ) and robustness (i.e., $\pm 2\sigma_{\bar{x}}$) among all rotation amplitude than low-cost u-blox receivers. Secondly, by comparing GPS only and the GPS + Galileo solution, an improvement in precision could be detected with the inclusion of the Galileo
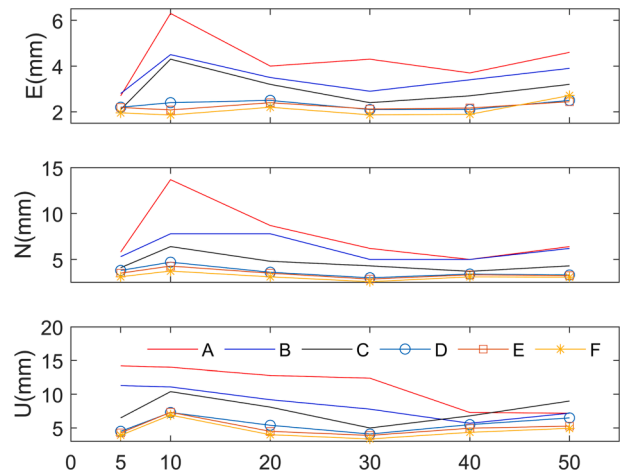
Fig. 15. E/N/U precision for case A-F for different rotation radii shows a general increase in precision from case A-F.

constellation. The margin ($\pm 2\sigma_{\bar{x}}$) also suggests that the GPS + Galileo precisions are more consistent and robust for different rotation amplitudes than GPS only solution. Thirdly, the time-series when the base antenna is adopted generally displays worse precision than the AS10 base antenna.

Similar conclusions could be made from Table 6 with analyses of *E/N/U* residuals except for the vertical displacement residuals, where the achieved precision with patch base antenna could be better than that with AS10, probably due to uncalibrated antenna parameters as described in Hamza et al. [31], since the uncalibrated phase centre variations (PCV) can cause serious errors on the vertical components [66].

To improve the precision of low-cost GNSS measurement, strategies by integrating the two closely spaced low-cost rovers are devised. An improved *E/N/U* measurement precision could be obtained by the average combination of the two low-cost time-series, leading to up to 1.7 mm improvement for the *E/N* component and up to 3.1 mm for the *Up* component (Fig. 15 radius 10 cm, case C to D). This finding confirms the effect of noise reduction by averaging, as shown by Jo et al. [16]. The strategies to mitigate the low-frequency systematic noise are also attempted by CME and high pass filtering. It has been proved that mainly high-pass filtering, but also CME to some extent, strategies by averaging the filtered time-series lead to more precise results with a precision improvement up to 0.7 mm and 0.2 mm in the *Up* component, respectively (Table 7).

Fig. 15 shows the precision improvement from scenario A to scenario F for different rotation radii. It is indicated that the precision improvement for *E/N* components is mainly (more than 68% of the total improvement) attributed to (i) the incorporation of the Galileo constellation, (ii) adopting a higher-quality base antenna, and (iii) the

Table 6
Precision of E/N/U estimation, expressed as in Table 5, based on tests of different rotation radii and GPS only and GPS + Galileo solutions.

Base antenna	Rover	The precision of E/N/U estimation (mm) ($\mu \pm 2\sigma_{\bar{x}}$)					
		E		N		U	
		G	G + E	G	G + E	G	G + E
AS10	Leica	2.4 ± 0.4	1.8 ± 0.3	3.6 ± 0.6	2.6 ± 0.2	4.2 ± 0.6	2.9 ± 0.3
	U-blox 1	3.8 ± 0.9	2.9 ± 0.5	6.6 ± 1.8	4.6 ± 0.9	10.0 ± 3.7	6.9 ± 1.7
	U-blox 3	4.0 ± 0.7	3.0 ± 0.3	7.7 ± 2.3	5.6 ± 1.3	9.4 ± 2.6	6.6 ± 1.3
Patch	Leica	2.6 ± 0.3	2.4 ± 0.3	3.9 ± 0.5	2.9 ± 0.4	3.2 ± 0.3	2.3 ± 0.1
	U-blox 1	4.2 ± 0.9	3.5 ± 0.5	7.4 ± 2.3	6.1 ± 0.9	9.8 ± 2.2	7.6 ± 1.6
	U-blox 3	3.8 ± 0.7	3.2 ± 0.4	7.3 ± 1.9	6.0 ± 1.1	9.8 ± 2.6	7.7 ± 2.2

Table 7

Precision improvement for E/N/U component by different approaches using as representative case the test of rotation radius of 30 cm.

Cases		Precision (mm)		
		E	N	U
A	U-blox 1 GPS-only solution with patch base antenna	4.3	6.2	12.4
B	U-blox 1 GPS + Galileo solution with patch base antenna	2.9	5.0	7.8
C	U-blox 1 GPS + Galileo solution with AS10 base antenna	2.4	4.3	5.0
D	Combined GPS + Galileo solutions by averaging u-blox 1 and u-blox 3 initial time-series with AS10 base antenna	2.1	3.0	4.1
E	Applying the CME filter to two lost-cost GPS + Galileo time-series and then averaging the two CME filtered time-series	2.1	2.9	3.9
F	Applying the high-pass filter to two low-cost GPS + Galileo time-series and then averaging the two high-pass filtered time-series	1.9	2.6	3.4
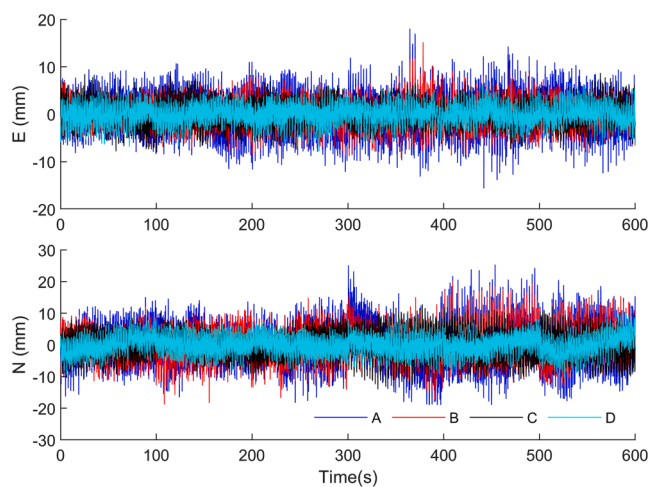
Fig. 16. E/N/U residual time-series for case A-D for 30 cm rotation radius shows a general increase in precision from case A to D.

average combination, which leads up to 9 mm improvement (Northing component for 10 cm radius, from A to D). However, the improvement from CME and high-pass filter is about 10% of the total precision improvement within ~1 mm in most cases. For the *Up* components, the precision from scenario B seems better than scenario C with the radius of 40 cm and 50 cm, probably due to the uncalibrated patch antenna parameters as aforementioned.

In Fig. 16, the *E/N* residuals time-series for 30 cm rotation radius for scenario A-D is illustrated in correspondence to Table 7. It is shown that for *E/N* residuals, the successive improvement of precision from scenario A to scenario D, which reduces the Eastings residuals standard deviation from 4.3 mm to 2.1 mm and Northings residuals standard deviations from 6.2 mm to 3 mm.

10. Case study: monitoring wilford pedestrian suspension bridge using low-cost GNSS receivers

To assess the performance of the low-cost GNSS rover in a real monitoring scenario, a bridge trial (Fig. 17) was conducted. The low-cost GNSS sensors were deployed at Wilford Suspension Bridge, Nottingham, to monitor the bridge response and derive its modal frequencies when subjected to human-imposed excitations. The evaluation of the low-cost GNSS receiver was based on the comparison with the measurements of Robotic Total Station (RTS) and survey-grade GNSS receivers (Leica GS10-AS10). In the experiment, the low-cost u–blox rovers, survey-grade Leica rover, and 360° prismatic targets were all mounted at the midspan of the bridge. The GNSS base station and RTS were established at the stable riverbank, at a distance of around 50 m from the midspan of

the bridge and recorded with 10 Hz sampling rate. The excitation of the bridge was imposed by a group of people by designated loading activities, including jumping, walking, and marching.

After data acquisition and processing, the low-cost GNSS, geodetic GNSS, and RTS results were analysed both in the time domain and frequency domain. The most well-detected response of the bridge corresponded to excitation produced by the synchronised jumping of a group of six people for about 60 s, in accordance with the excitation which were applied in previous similar studies [3,61,62]. Fig. 18 presents the *Up* component time-series of the RTS, the geodetic GNSS receiver, and the low-cost GNSS receiver and the corresponding spectra of a representative jumping excitation. Both GNSS time-series were derived after applying a high-pass filter to reduce the long-period noise. Based on the time-series, it is evident that the low-cost GNSS receiver time-series is noisier than the RTS and the Leica GNSS receiver, with the difference (RMSE) between u-blox and Leica not exceeding 3 mm.

Regarding the spectra derived from the spectral analysis of the *Up* component time-series, it is observed that the main modal frequency of the bridge, ~1.680 Hz, was clearly detected in all spectra, with the difference between the low-cost GNSS spectrum and the other two spectra (RTS and GNSS Leica) not exceeding 0.02 Hz. The derived modal frequency is in agreement with the modal frequency derived in previous studies [61,62]. Generally, by examining the spectra from different loading events, it was shown that the derived frequencies are almost identical (within 0.02 Hz difference) between low-cost GNSS, geodetic GNSS, and RTS measurements, indicating that the low-cost GNSS receivers can be used to identify the dynamic response and the main modal frequencies of the bridge.

11. Conclusion

In this research, we evaluated the performance of a low-cost mass-market GNSS receiver in dynamic displacement monitoring and explored the possibility of precision enhancement by adopting another receiver of the same model in close vicinity under favourable measurement conditions. A following case study was conducted to assess the feasibility of using the low–cost GNSS stations in a real bridge SHM scenario. It could be concluded that; (i) the major contribution of the base station on the precision improvement of the low-cost GNSS receiver is from the base antenna other than the receiver; (ii) as for dynamic displacement monitoring, multi-GNSS observation enhances the precision of the horizontal displacement estimation, reaching the level of 3–5 mm; (iii) the precision of the estimation of the horizontal displacement can be further improved by combining two closely-spaced low-cost GNSS receivers, with the high-pass filtering strategy resulting to the highest precision reaching the level of 2–3 mm; (iv) both major modal frequencies regarding the rotation experiment (~0.362 Hz) and the case study (~1.680 Hz) could be retrieved accurately with low-cost GNSS receivers compared to survey-grade GNSS receivers or RTS. Moreover, the time-series differences (RMSE) between the low-cost and survey-grade GNSS receivers are within 3 mm for the case study. Based on the experiments it was shown that low-cost GNSS receivers can be used to monitor dynamic motion of flexible civil engineering structures (e.g., long-span bridges, tall buildings, etc. [16,36,37,38]), with response amplitude up to a few dm [6,9], and also for other dynamic motion application, such as ground motion with long- and short-period frequencies (e.g., seismic motion; [5,11,67]). The promising experimental results were also confirmed with case study of Wilford Suspension bridge. The results of the current study are also in accordance with similar other studies focusing on PPP solutions of low-cost GNSS receivers for positioning and geomonitoring application [10,11]. Therefore, further investigation is needed to identify more sophisticated techniques, such as applying restriction using the distance of the two closely-spaced GNSS receivers to improve further the low-cost GNSS performance in monitoring dynamic motion or using more satellite systems (e.g., BeiDou, GLONASS) to improve the performance of low-

Fig. 17. A: Leica AS10 antenna & reflective prism underneath the GNSS antenna mounted at the midspan of the bridge, **B:** Two low-cost patch antennas with the same azimuth orientation at the midspan of the bridge, **C:** Low-cost GNSS receivers, raspberry pi models and power banks connected to the patch antennas in B.
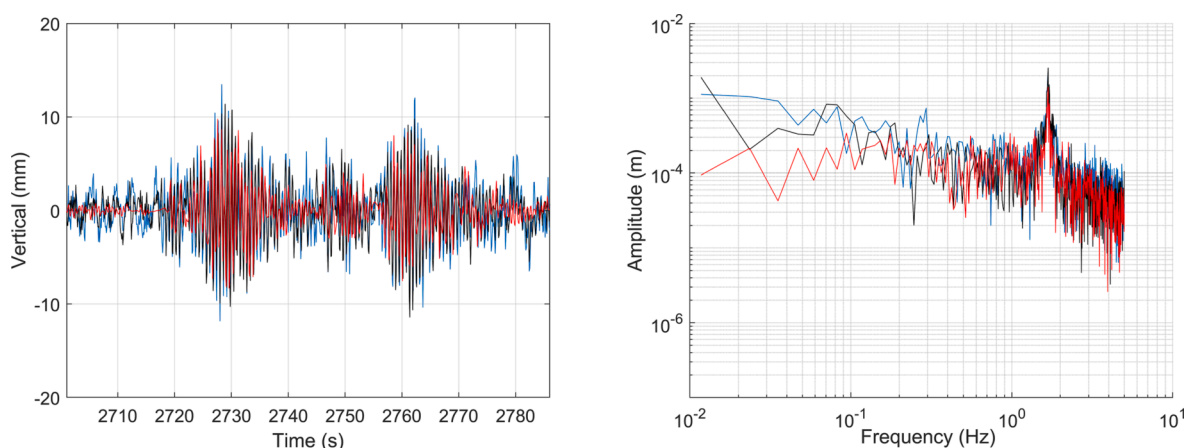
Fig. 18. (Left) High-pass filtered vertical time-series for RTS (Red), Leica (Black), and average combined u-blox 1 and u-blox 2 solutions (Blue) and **(Right)** corresponding DFT spectra, for excitation event 04.

cost GNSS receivers.

CRediT authorship contribution statement

Chenyu Xue: Methodology, Investigation, Software, Writing – original draft, Writing – review & editing, Visualization, Formal analysis. **Panos A. Psimoulis:** Methodology, Resources, Conceptualization, Supervision, Writing – review & editing. **Xiaolin Meng:** Resources, Supervision.

Declaration of Competing Interest

The authors declare that they have no known competing financial interests or personal relationships that could have appeared to influence

the work reported in this paper.

Acknowledgement

Appendix A. Supplementary material

Supplementary data to this article can be found online at https://doi.org/10.1016/j.measurement.2022.111819.

References

[1] P. Psimoulis, S. Pytharouli, D. Karambalis, S. Stiros, Potential of Global Positioning System (GPS) to measure frequencies of oscillations of engineering structures, J. Sound Vib. 318 (3) (2008) 606–623.

[2] T.-H. Yi, H.-N. Li, M. Gu, Recent research and applications of GPS-based monitoring technology for high-rise structures, Struct. Control Health Monitor. 20 (5) (2013) 649–670.

[3] F. Moschas, S. Stiros, Measurement of dynamic displacement and of the modal frequencies of a short-span pedestrian bridge using GPS and an accelerometer, Eng. Struct. 33 (1) (2011) 10–17.

[4] S. Häberling, M. Rothacher, Y. Zhang, J.F. Clinton, A. Geiger, Assessment of high-rate GPS using a single-axis shake table, J. Geod. 89 (7) (2015) 697–709.

[5] P.A. Psimoulis, N. Houlié, M. Habboub, C. Michel, M. Rothacher, Detection of ground motions using high-rate GPS time-series, Geophys. J. Int. 214 (2) (2018) 1237–1251.

[6] X. Meng, D. Nguyen, Y. Xie, J. Owen, P. Psimoulis, S. Ince, Q. Chen, J. Ye, P. Bhatia, Design and implementation of a new system for large bridge monitoring—GeoSHM, Sensors 18 (3) (2018) 775, https://doi.org/10.3390/s18030775.

[7] H.A. Msaewe, P.A. Psimoulis, C.M. Hancock, G.W. Roberts, L. Bonenberg, Monitoring the response of Severn Suspension Bridge in the United Kingdom using multi-GNSS measurements, Struct. Control Health Monitor. 28 (11) (2021), https://doi.org/10.1002/stc.v28.1110.1002/stc.2830.

[8] T. Yi, H. Li, M. Gu, Recent research and applications of GPS based technology for bridge health monitoring, Sci. China Technol. Sci. 53 (10) (2010) 2597–2610.

[9] X. Meng, D.T. Nguyen, J.S. Owen, Y. Xie, P. Psimoulis, G. Ye, Application of GeoSHM system in monitoring extreme wind events at the forth Road Bridge, Rem. Sens. 11 (23) (2019) 2799.

[10] Z. Nie, F. Liu, Y. Gao, Real-time precise point positioning with a low-cost dual-frequency GNSS device, GPS Solut. 24 (1) (2020) 1–11.

[11] R. Hohensinn, R. Stauffer, I.D.H. Pinzon, R. Spannagel, A. Wolf, Y. Rossi, M. Rothacher, Low-cost vs. Geodetic-grade GNSS Instrumentation: Geomonitoring with High-rate and Real-time PPP, in: Proceedings of the 34th International Technical Meeting of the Satellite Division of The Institute of Navigation (ION GNSS+ 2021), 2021, pp. 3990–4001.

[12] T. Takasu, A. Yasuda, Evaluation of RTK-GPS performance with low-cost single-frequency GPS receivers, in: Proceedings of international symposium on GPS/GNSS, 2008, pp. 852–861.

[13] T. Takasu, A. Yasuda, Development of the low-cost RTK-GPS receiver with an open source program package RTKLIB Vol. 1 (2009).

[14] A. Cina, M. Piras, Performance of low-cost GNSS receiver for landslides monitoring: test and results, Geom. Nat. Hazards Risk 6 (5–7) (2015) 497–514.

[15] M.S. Garrido-Carretero, M.C. de Lacy-Pérez de los Cobos, M.J. Borque-Arancón, A. M. Ruiz-Armenteros, R. Moreno-Guerrero, A.J. Gil-Cruz, Low-cost GNSS receiver in RTK positioning under the standard ISO-17123-8: a feasible option in geomatics, Measurement 137 (2019) 168–178.

[16] H. Jo, S.-H. Sim, A. Tatkowski, B.F. Spencer, M.E. Nelson, Feasibility of displacement monitoring using low-cost GPS receivers, Struct. Control Health Monitor. 20 (9) (2013) 1240–1254.

[17] L. Biagi, F.C. Grec, M. Negretti, Low-cost GNSS receivers for local monitoring: experimental simulation, and analysis of displacements, Sensors 16 (12) (2016) 2140.

[18] S. Caldera, E. Realini, R. Barzaghi, M. Reguzzoni, F. Sansò, Experimental study on low-cost satellite-based geodetic monitoring over short baselines, J. Surv. Eng. 142 (3) (2016) 04015016.

[19] L. Poluzzi, L. Tavasci, F. Corsini, M. Barbarella, S. Gandolfi, Low-cost GNSS sensors for monitoring applications, Appl. Geom. 12 (S1) (2020) 35–44.

[20] L. Lu, L. Ma, T. Wu, X. Chen, Performance analysis of positioning solution using low-cost single-frequency u-blox receiver based on baseline length constraint, Sensors 19 (19) (2019) 4352.

[21] L. Zhang, V. Schwieger, Investigation of a L1-optimized choke ring ground plane for a low-cost GPS receiver-system, J. Appl. Geodesy 12 (1) (2018) 55–64.

[22] R. Odolinski, P.J.G. Teunissen, Single-frequency, dual-GNSS versus dual-frequency, single-GNSS: a low-cost and high-grade receivers GPS-BDS RTK analysis, J. Geod. 90 (11) (2016) 1255–1278.

[23] R. Odolinski, P.J.G. Teunissen, Low-cost, high-precision, single-frequency GPS–BDS RTK positioning, GPS Solut. 21 (3) (2017) 1315–1330.

[24] R. Odolinski, P.J.G. Teunissen, Low-cost, 4-system, precise GNSS positioning: a GPS, Galileo, BDS and QZSS ionosphere-weighted RTK analysis, Meas. Sci. Technol. 28 (12) (2017) 125801, https://doi.org/10.1088/1361-6501/aa92eb.

[25] R. Odolinski, P.J.G. Teunissen, An assessment of smartphone and low-cost multi-GNSS single-frequency RTK positioning for low, medium and high ionospheric disturbance periods, J. Geod. 93 (5) (2019) 701–722.

[26] R. Odolinski, P.J. Teunissen, Best integer equivariant estimation: performance analysis using real data collected by low-cost, single-and dual-frequency, multi-GNSS receivers for short-to long-baseline RTK positioning, J. Geod. 94 (9) (2020) 1–17.

[27] T. Kersten, J.A. Paffenholz, Feasibility of consumer grade GNSS receivers for the integration in multi-sensor-systems, Sensors 20 (9) (2020) 2463.

[28] C. Xue, P. Psimoulis, Q. Zhang, X. Meng, Analysis of the performance of closely spaced low-cost multi-GNSS receivers, Appl. Geom. 13 (3) (2021) 415–435.

[29] L. Zhang, V. Schwieger, Improving the quality of low-cost GPS receiver data for monitoring using spatial correlations, J. Appl. Geodesy 10 (2) (2016) 119–129.

[30] T. Bellone, P. Dabove, A.M. Manzino, C. Taglioretti, Real-time monitoring for fast deformations using GNSS low-cost receivers, Geom. Nat. Hazards Risk 7 (2) (2016) 458–470.

[31] V. Hamza, B. Stopar, T. Ambrožič, G. Turk, O. Sterle, Testing multi-frequency low-cost GNSS receivers for geodetic monitoring purposes, Sensors 20 (16) (2020) 4375.

[32] L. Tunini, D. Zuliani, A. Magrin, Applicability of cost-effective GNSS sensors for crustal deformation studies, Sensors 22 (1) (2022) 350.

[33] E. Benedetti, R. Ravanelli, M. Moroni, A. Nascetti, M. Crespi, Exploiting performance of different low-cost sensors for small amplitude oscillatory motion monitoring: preliminary comparisons in view of possible integration, J. Sens. 2016 (2016) 1–10.

[34] A.M. Lăpădat, C.C. Tiberius, P.J. Teunissen, Experimental evaluation of smartphone accelerometer and low-cost dual frequency GNSS sensors for deformation monitoring, Sensors 21 (23) (2021) 7946.

[35] N. Manzini, A. Orcesi, C. Thom, M.-A. Brossault, S. Botton, M. Ortiz, J. Dumoulin, Performance analysis of low-cost GNSS stations for structural health monitoring of civil engineering structures, Struct. Infrastruct. Eng. 18 (5) (2022) 595–611.

[36] A. Nickitopoulou, K. Protopsalti, S. Stiros, Monitoring dynamic and quasi-static deformations of large flexible engineering structures with GPS: accuracy, limitations and promises, Eng. Struct. 28 (10) (2006) 1471–1482.

[37] P. Breuer, T. Chmielewski, P. Górski, E. Konopka, Application of GPS technology to measurements of displacements of high-rise structures due to weak winds, J. Wind Eng. Ind. Aerodyn. 90 (3) (2002) 223–230.

[38] X. Tang, X. Li, G.W. Roberts, C.M. Hancock, H. de Ligt, F. Guo, 1 Hz GPS satellites clock correction estimations to support high-rate dynamic PPP GPS applied on the Severn suspension bridge for deflection detection, GPS Solut. 23 (2) (2019) 1–12.

[39] P.A. Psimoulis, S.C. Stiros, Measurement of the dynamic displacements and of the modal frequencies of a short-span pedestrian bridge using GPS and an accelerometer, Eng. Struct. 23 (5) (2008) 389–403.

[40] F. Moschas, S. Stiros, Measurement of the dynamic displacements and of the modal frequencies of a short-span pedestrian bridge using GPS and an accelerometer, Eng. Struct. 33 (1) (2011) 10–17.

[41] L. Zhang, V. Schwieger, Reducing multipath effect of low-cost GNSS receivers for monitoring by considering temporal correlations, J. Appl. Geodesy 14 (2) (2020) 167–175.

[42] M. Habboub, P.A. Psimoulis, R. Bingley, M. Rothacher, A multiple algorithm approach to the analysis of GNSS coordinate time series for detecting geohazards and anomalies, J. Geophys. Res.: Solid Earth 125 (2) (2020) e2019JB018104.

[43] J.K. Ray, M.E. Cannon, P. Fenton, GPS code and carrier multipath mitigation using a multiantenna system, IEEE Trans. Aerosp. Electron. Syst. 37 (1) (2001) 183–195.

[44] K.S. Vishvaksenan, K. Mithra, R. Kalaiarasan, K.S. Raj, Mutual coupling reduction in microstrip patch antenna arrays using parallel coupled-line resonators, IEEE Anten. Wirel. Propag. Lett. 16 (2017) 2146–2149.

[45] U-blox AG, U-blox M8 concurrent GNSS timing modules. 2020. <https://content.u-blox.com/sites/default/files/NEO-LEA-M8T-FW3_DataSheet_%28UBX-150 25193%29.pdf> (Accessed 13 August 2022).

[46] U-blox AG, Zed-F9P-04B Data Sheet. 2022. <https://content.u-blox.com/sites/default/files/ZED-F9P-04B_DataSheet_UBX-21044850.pdf> (Accessed 13 August 2022).

[47] N. Shen, L. Chen, J. Liu, L. Wang, T. Tao, D. Wu, R. Chen, A review of global navigation satellite system (GNSS)-based dynamic monitoring technologies for structural health monitoring, Rem. Sens. 11 (9) (2019) 1001.

[48] L.H. Estey, C.M. Meertens, TEQC: the multi-purpose toolkit for GPS/GLONASS data, GPS Solut. 3 (1) (1999) 42–49.

[49] T. Everett, RTKLIB code: Windows Executables. 2020. <http://rtkexplorer.com/downloads/rtklib-code> (Accessed 28 June 2022).

[50] T. Everett, Documentation of differences between RTKLIB demo5 and RTKLIB 2.4.3. 2016. <http://rtkexplorer.com/downloads/rtklib-code/documentation-of-differences-between-rtklib-demo5-and-rtklib-2-4-3/> (Accessed 13 August 2022).

[51] P.J.G. Teunissen, The least-squares ambiguity decorrelation adjustment: a method for fast GPS integer ambiguity estimation, J. Geod. 70 (1-2) (1995) 65–82.

[52] X.-W. Chang, X. Yang, T. Zhou, MLAMBDA: a modified LAMBDA method for integer least-squares estimation, J. Geod. 79 (9) (2005) 552–565.

[53] T. Takasu, RTKLIB ver. 2.4. 2 Manual. RTKLIB: An Open Source Program Package for GNSS Positioning, 29, 49, 2013.

[54] L. Wanninger, Carrier-phase inter-frequency biases of GLONASS receivers, J. Geod. 86 (2) (2012) 139–148.

[55] H.A. Msaewe, C.M. Hancock, P.A. Psimoulis, G.W. Roberts, L. Bonenberg, H. de Ligt, Investigating multi-GNSS performance in the UK and China based on a zero-baseline measurement approach, Measurement 102 (2017) 186–199.

[56] V. Pratt, Direct least-squares fitting of algebraic surfaces, ACM SIGGRAPH Comput. Graph. 21 (4) (1987) 145–152.

[57] N. Chernov, Circle Fit (Pratt method), MATLAB Central File Exchange, 2021. <https://www.mathworks.com/matlabcentral/fileexchange/22643-circle-fit-pratt-method> (Accessed 10 July 2022).

[58] P. Seibold, Sine fitting, MATLAB Central File Exchange, 2021. <https://www.mathworks.com/matlabcentral/fileexchange/66793-sine-fitting> (Accessed 10 July 2022).

[59] G.J. Wakileh, Harmonics in rotating machines, Electr. Power Syst. Res. 66 (1) (2003) 31–37.

[60] C. Xiong, H. Lu, J. Zhu, Operational modal analysis of bridge structures with data from GNSS/accelerometer measurements, Sensors 17 (3) (2017) 436.

[61] J. Yu, X. Meng, X. Shao, B. Yan, L. Yang, Identification of dynamic displacements and modal frequencies of a medium-span suspension bridge using multimode GNSS processing, Eng. Struct. 81 (2014) 432–443.

[62] I. Peppa, P. Psimoulis, X. Meng, Using the signal-to-noise ratio of GPS records to detect motion of structures, Struct. Control Health Monitor. 25 (2) (2018) e2080, https://doi.org/10.1002/stc.v25.210.1002/stc.2080.

[63] K. Choi, A. Bilich, K.M. Larson, P. Axelrad, Modified sidereal filtering: Implications for high-rate GPS positioning, Geophys. Res. Lett. 31 (22) (2004), https://doi.org/10.1029/2004GL021621.

[64] C.J. Benton, C.N. Mitchell, Isolating the multipath component in GNSS signal-to-noise data and locating reflecting objects, Radio Sci. 46 (06) (2011) 1–11.

[65] C. Ogaja, C. Satirapod, Analysis of high-frequency multipath in 1-Hz GPS kinematic solutions, GPS Solut. 11 (4) (2007) 269–280.

[66] M. Rothacher, S. Schaer, L. Mervart, G. Beutler, Determination of antenna phase center variations using GPS data, in: Proc. IGS Workshop on Special Topics and New Directions, IGS, 1995, pp. 205–220.

[67] P.A. Psimoulis, N. Houlie, C. Michel, M. Meindl, M. Rothacher, Long-period surface motion of the multipath M_w9.0 Tohoku-Oki earthquake, Geophys. J. Int. 199 (2) (2014) 968–980.